Journal of Power Sources 700 (2027) 241946

Contents lists available at ScienceDirect

Journal of Power Sources

journal homepage: www.elsevier.com/locate/jpowsour

Mapping the impact of imide-type anions on morphology and ion transport properties in PEO-based polymer electrolytes for potassium batteries

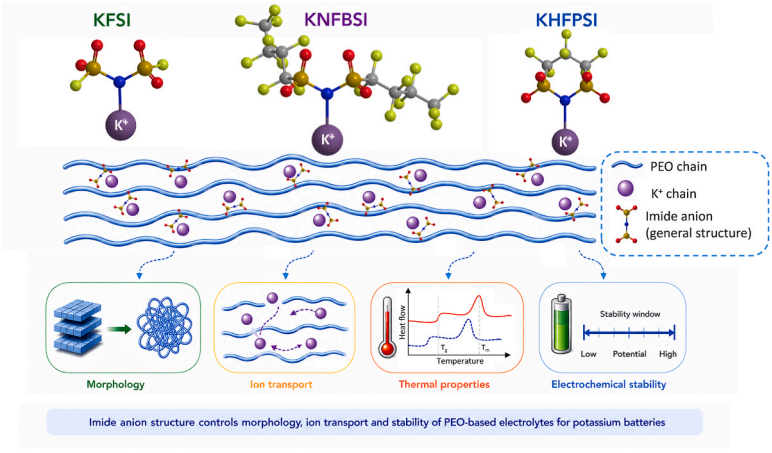
Timofey I. Kolesnikov [a,b,*], Hongyuan Yu [a], Ramon Zimmermanns [a,c], Mareen Schaller [a], Liuda Mereacre [a], Arseniy Bokov [a], Sylvio Indris [a], Michael Knapp [a], Patrick Theato [b,d], Fabian Jeschull [a]

[a] Karlsruhe Institute of Technology (KIT), Institute for Applied Materials - Energy Storage Systems (IAM-ESS), Hermann-von-Helmholtz-Platz 1, Eggenstein-Leopoldshafen, 76344, Germany
[b] Karlsruhe Institute of Technology (KIT), Institute for Chemical Technology and Polymer Chemistry (ITCP), Engesserstraße 18, Karlsruhe, 76131, Germany
[c] Helmholtz Institute Ulm (HIU), Helmholtzstraße 11, Ulm, 89081, Germany
[d] Karlsruhe Institute of Technology (KIT), Soft Matter Synthesis Laboratory, Institute for Biological Interfaces III (IBG-3), Hermann-von-Helmholtz-Platz 1, Eggenstein-Leopoldshafen, 76344, Germany

HIGHLIGHTS

- Potassium salts with different anions change solid polymer electrolyte morphology.
- Secondary crystalline phases hinder potassium-ion transport.
- The best-performing potassium salt enables stable cycling of potassium metal cells.

GRAPHICAL ABSTRACT



ARTICLE INFO

Keywords:
Solid polymer electrolyte
PEO
Potassium metal batteries
Ion transport

ABSTRACT

The transition from liquid electrolytes to solid polymer electrolytes (SPEs) is a promising approach to improve the safety and stability of potassium metal batteries (PMBs). While Poly(ethylene oxide) (PEO) is widely used in SPEs, the effect of potassium salts on structure and performance of SPEs in PMBs have not been systematically studied. In this work, three salts, namely potassium bis(fluorosulfonyl)imide (KFSI), potassium bis(nonafluorobutanesulfonyl)imide (KNFBSI), and potassium hexafluoropropane-1,3-disulfonimide (KHFPSI), were studied over a wide compositional range. Thermal and structural characterization using DSC and XRD reveals

* Corresponding author. Karlsruhe Institute of Technology (KIT), Institute for Applied Materials - Energy Storage Systems (IAM-ESS), Hermann-von-Helmholtz-Platz 1, Eggenstein-Leopoldshafen, 76344, Germany
E-mail address: timofey.kolesnikov@kit.edu (T.I. Kolesnikov).

https://doi.org/10.1016/j.jpowsour.2026.241946
Received 18 August 2026; Received in revised form 8 October 2026; Accepted 6 November 2026
Available online 16 November 2026
0378-7753/© 2026 The Authors. Published by Elsevier B.V. This is an open access article under the CC BY license (http://creativecommons.org/licenses/by/4.0/).
Open access funding enabled and organized by Projekt DEAL.

that all systems exhibit a decrease in crystallinity with increasing salt content, while KHFPSI enables nearly complete amorphization of PEO at high salt loadings. Ionic conductivities on the order of 10^{-3} S cm^{-1} were achieved at elevated temperatures (60-70 °C) for all systems, yet significant differences were observed at lower temperatures. The SPEs containing KNFBSI exhibit strongly suppressed conductivity, which is attributed to the formation of additional crystalline phases. ^{19}F NMR measurements confirm the presence of immobile ionic species in KNFBSI-containing systems, which are attributed to these secondary crystalline phases and lead to reduced ion transport. In contrast, KFSI-based SPEs exhibit the highest ionic conductivity due to the small size and high mobility of the anion.

1. Introduction

The global development in energy-storage systems requires transition beyond lithium-based technologies, due to its limited availability and high cost [1,2]. In this context, potassium has emerged as an attractive alternative to lithium due to its abundancy, low cost, and offers favorable electrochemical characteristics [3–5]. For example, the K^+/K redox potential in carbonate-based electrolytes is approximately 0.15 – 0.20 V more negative than Li^+/Li, enabling high energy density, while its natural abundance makes it suitable for large-scale, cost-effective battery systems [6–8]. However, liquid electrolytes commonly used in potassium batteries face serious challenges. The highly reactive nature of potassium metal can trigger parasitic reactions at the interface, leading to unstable solid-electrolyte interphase (SEI), rapid capacity fading, and overall safety issues [9–11]. These drawbacks significantly limit the cycle life and practicality of PMBs. A promising strategy to address these challenges is the use of SPEs, which are non-flammable and exhibit enhanced electrochemical and mechanical stability [12,13]. As a result, they are less susceptible to decomposition reactions and improve the overall safety of the battery.

SPEs are typically composed of a polymer matrix and a conducting salt [14,15]. Among the various polymers investigated for SPEs, PEO remains one of the most extensively studied and widely used materials due to its ability to efficiently dissolve many inorganic salts and its relatively low glass transition temperature, which promotes ion mobility [16–18]. In addition, PEO was the first polymer utilized as an SPE and found commercial application in lithium metal batteries, demonstrating its effectiveness [19]. Although a range of polymers, including polycarbonates [20], polyacrylonitrile [21], and poly(vinyl alcohol) [22] have been employed as SPEs, PEO remains the benchmark for solid-state lithium metal batteries. In the case of PMB, only a very limited number of polymer electrolytes beyond PEO have so far demonstrated stable long-term cycling in full cells against cathode materials such as $K_2Fe[Fe(CN)_6]$. Moreover, it has been shown that due to the high reactivity of potassium metal, ester groups in polymers such as polycaprolactone are prone to depolymerization, significantly limiting the choice of suitable polymers for SPEs in PMB [23]. Therefore, PEO remains thus far the most favorable option for utilization in SPEs.

The second important component of SPEs is the conducting salt, in which the anion can be synthetically tailored, enabling systematic tuning of electrolyte properties [24–28]. In potassium-based SPEs, KFSI is the most commonly chosen salt due to its good dissociation behavior and compatibility with PEO [29–32]. Additionally, KFSI is prone to decomposition because of its limited stability, and the resulting decomposition products are known to stabilize the SEI [29]. Nevertheless, relying solely on KFSI may limit further improvements in SPEs development. Different salts can strongly influence both the composition and stability of the SEI layer formed on potassium metal, which is crucial for achieving stable long-term cycling. Beyond interfacial effects, the choice of conductive salt also strongly impacts the polymer morphology, by acting as plasticizers for the polymer matrix, reducing its crystallinity and glass transition temperature while increasing polymer chain mobility [33,34]. Moreover, PEO–salt interactions can lead to the formation of secondary crystalline phases, which directly impact ionic conductivity, mechanical properties, and overall electrochemical behavior [27,28,34–37]. Therefore, it is essential to systematically investigate a broader range of potassium salts to understand how they influence both the polymer structure and cycling behavior. Such studies can help to identify the optimal salt–polymer combinations that balance ionic conductivity, interfacial stability, and mechanical properties, facilitating the development of high-performance solid polymer electrolytes for PMBs.

In a previous study, it has been demonstrated that potassium bis(trifluoromethane sulfonyl)imide enables stable cycling as a salt for SPEs in PMB, achieving 90% capacity retention over 50 cycles when potassium iron hexacyanoferrate ($K_2Fe[Fe(CN)_6]$) is used as positive electrode [38]. The focus of this study is to understand the impact of selected sulfonyl imide conducting salts with different fluorinated substituents on the physical properties of polymer electrolytes. To this end, a complementary approach was used to combine DSC, solid-state NMR, and temperature-dependent XRD for investigating the thermal and morphological properties, as well as ion mobility and salt dissociation. The obtained results highlight the superior performance of KFSI among the investigated conducting salts, particularly in terms of high ionic conductivity and capacity retention in PMB configurations. Furthermore, the exploration of alternative conducting salts reveals promising candidates that may serve as co-salts by enhancing electrochemical stability or reducing the degree of crystallinity, thereby offering additional pathways to tailor ion transport and interfacial stability.

2. Experimental part

2.1. Materials

Potassium bis(nonafluorobutanesulfonyl)imide (>98.0%, TCI) (KNFBSI), potassium bis(fluorosulfonyl)imide (KFSI) (>95.0%, TCI), potassium 1,1,2,2,3,3-hexafluoropropane-1,3-disulfonimide (KHFPSI) (>98.0%, TCI) and PEO ($M_w = 5{,}000{,}000$, Sigma-Aldrich) were dried at 110 °C for 12 h under vacuum (10^{-3} mbar) and transferred to the argon filled glovebox, where all following procedures were carried out under an inert atmosphere ($H_2O < 0.1$ ppm, $O_2 < 0.1$ ppm). Dry acetonitrile (99.8%, Sigma-Aldrich), *N*-methyl-2-pyrrolidone (NMP) (≥99%, Sigma-Aldrich), potassium hexacyanoferrate(II) trihydrate (≥98.5%, Sigma-Aldrich), iron(II) sulfate heptahydrate (≥98.5%, Sigma-Aldrich), polyvinylpyrrolidone ($M_w = 50{,}000$, Sigma-Aldrich) and trisodium citrate 5.5-hydrate (≥98.5%, Sigma-Aldrich), were purchased from Sigma-Aldrich (USA). Potassium metal (98% stored in mineral oil, Sigma-Aldrich) was transferred to the Ar-filled glovebox ($H_2O < 0.1$ ppm, $O_2 < 0.1$ ppm), washed with hexane and further used under inert atmosphere. $K_2Fe[Fe(CN)_6]$ (KFF) was synthesized according to a previously reported procedure [38].

2.2. Analytical methods

Attenuated total reflectance-Fourier transform infrared (ATR-FTIR) spectra were recorded in the range of 4000–400 cm^{-1} on a Bruker Vector 22 spectrometer.

Differential scanning calorimetry (DSC) thermograms were recorded using TA DSC Q200 (USA) with heating rates of 10 °C min^{-1} in nitrogen atmosphere. The degree of crystallinity (X_c) was calculated using

equation (1), where ΔH_{peo} is enthalpy of melting of 100% crystalline PEO = 196.4 J/g and f_{peo} is weight fraction of PEO in SPE [39,40]. ΔH_m and ΔH_c correspond to the enthalpy of melting and cold crystallization.

$$X_c = \frac{\Delta H_m - \Delta H_c}{\Delta H_{peo} * f_{peo}} * 100\% \quad \text{(eq. 1)}$$

The samples were heated up to 150 °C and cooled down to −70 °C at a heating rate of 20 °C min^{-1} before the measurements.

^{1}H NMR spectra were recorded using a Bruker Ascend 400 NMR spectrometer (Germany) with a working frequency of 400 MHz. $CDCl_3$ was used as solvent in NMR experiments.

Thermogravimetric analysis (TGA) was performed using TA TG5500 thermobalance (USA) at a heating rate of 10 °C min^{-1} up to 700 °C under nitrogen flow of 100 mL min^{-1}.

X-ray diffraction (XRD) measurements of the polymer films were performed using a STOE STADI-P diffractometer (Germany) equipped with a KIT-designed sample holder with programmable temperature and Ag-Kα_1 radiation ($\lambda = 0.5594$ Å) in transmission geometry. The measurements were performed over a 2θ range of 0-36° using a linear MYTHEN2 detector with 0.015° resolution. For temperature-dependent analysis, the SPE samples were crimped into coin cells with glass windows. Prior to data collection, the samples were heated to 70 °C and subsequently cooled to 20 °C in order to erase their thermal history. At each measurement temperature within the range of 20–70 °C, the samples were equilibrated for 1 h before recording the diffractograms. The degree of crystallinity X_c was calculated using equation (2), where $A_{crystalline}$ and A_{total} correspond to the integral area of the crystalline reflections and the total scattering area, respectively.

$$Xc = \frac{A_{crystalline}}{A_{total}} \quad \text{(eq. 2)}$$

Temperature-dependent ^{19}F pulsed-field gradient (PFG) NMR measurements were performed on a Bruker Avance spectrometer at a magnetic field of 7.05 T, using a PFG probe with a maximal gradient strength of 30 T/m. The samples were investigated using a stimulated-echo pulse. The gradient duration was set to 1.5 ms and a diffusion time of 150 ms was chosen. The recycle delay was always well above five times the spin-lattice relaxation time. All samples were sealed in 5 mm evacuated borosilicate glass tubes and measured between 27 and 67 °C in 5 K steps.

With PFG NMR the long-range transport of ions can be analyzed by varying the applied gradient field strength g. The recorded echo intensity $I(g)$ of the ^{19}F spectra is described by the Stejskal and Tanner [41] equation (3):

$$I = I_0 \cdot \exp\left(- D\gamma^2\delta^2 g^2 \left(\Delta - \frac{\delta}{3}\right)\right) \quad \text{(eq. 3)}$$

where δ is the length of the gradient pulse, Δ the diffusion time and the γ magnetogyric ratio.

2.3. Positive electrode preparation

For the preparation of positive electrodes for electrochemical tests, 180 mg $K_2Fe[Fe(CN)_6]$, 90 mg carbon black super C65 (TIMCAL), 30 mg poly(vinylidene fluoride) (HSV900, Kynar), 30 mg PEO and 1 ml NMP were placed in a ball-mill container. The container was transferred to a ball-mill mixer SPEX 8000, and the slurry was mixed for 20 min. An additional 0.5 mL of NMP was added, and the slurry was mixed for another 20 min. Subsequently, the slurry was spread onto a conductive carbon-coated aluminum foil (MTI, 18 μm) using an automatic film applicator Zehntner ZAA 2300 with a gap width of 150 μm and dried after deposition at 60 °C. The mass loading was ~1.5 mg cm^{-2} (0.375 g cm^{-3}). The electrode sheets were calendared to a thickness of ~40 μm. Round-shaped electrodes with a diameter of 14 mm were cut out and dried at 110 °C for 12 h under vacuum prior to use.

2.4. Preparation of solid polymer electrolyte

The predefined amounts of PEO and potassium salt corresponding to the molar ratios of ethylene oxide (EO):K = 20:1, 18:1, 16:1, 14:1 and 12:1 were dissolved in dry acetonitrile (99.8%, Sigma-Aldrich) forming a homogeneous solution. The films were fabricated by casting solutions into Teflon molds, followed by acetonitrile evaporation at room temperature and then at 60 °C. Subsequently, the obtained films were additionally dried at 60 °C for 24 h under vacuum. The resulting films with a thickness of 100-150 μm were peeled off from the Teflon molds.

2.5. Electrochemical characterization

Electrochemical impedance spectroscopy (EIS) was measured using coin-type cells (2032-type round button cell) that were assembled in an Ar-filled glovebox. Polymer films with a diameter of 10 mm were sandwiched between two stainless steel (SS) electrodes and measured using a VSP potentiostat (BioLogic Science Instruments, France) over a frequency range from 1 MHz to 500 mHz with an amplitude of 20 mV. All samples were preconditioned overnight, in a temperature chamber MK-56 (Binder, Germany) at 60 °C and then measured in temperature range between 20 and 70 °C with gradual temperature increase in steps of 10 °C. Each temperature was held constant for 2 h before recording the impedance spectra. Further, the bulk electrolyte resistance (R_b) was estimated from the Nyquist plot, and the ionic conductivity (σ) was calculated according to equation (4):

$$\sigma = \frac{1}{R_b} \cdot \frac{l}{A} \quad \text{(eq. 4)}$$

where l represents the thickness, and A represents the area of a SPE film.

Linear sweep voltammetry (LSV) was conducted at 55 °C from OCV to 6 V for a SS|SPE|K° cell with a scanning rate of 0.1 mVs^{-1}. The SPE and K metal electrodes had diameters of 17 and 14 mm, respectively. Galvanostatic cycling with potential limits (GCPL) of half-cells with configuration K°|SPE|KFF was performed in coin cells using a VMP-300 potentiostat (BioLogic Science Instruments, France) inside a KBF-130 temperature chamber (Binder, Germany) at 55 °C. The KFF, SPE, and K metal electrodes had diameters of 14, 17, and 14 mm, respectively. The K metal had a thickness of ~100 μm, corresponding to a theoretical areal capacity of ~5.90 mAh cm^{-2}. The cells containing different SPEs were preconditioned for 48 h at 60 °C before electrochemical measurements. All cells were cycled first at C/20 then C/10, C/5, C/2 and C/1 (1C = 155 mAh/g with respect to the theoretical capacity of KFF) for 5 cycles with cut-offs at 4.3 V and 2.5 V vs K^+/K. Afterwards cycling was continued at a rate of C/10.

3. Results and discussion

3.1. Salt characterization

The effect of three different conductive K^+ salts has been investigated in the present study, and the respective chemical structures of KFSI, KNFBSI and KHFPSI are shown in Fig. 1A. KFSI is the most commonly used salt in PMB that contains fluorine atoms attached to imide anion. KNFBSI contains longer fluorinated chain, which increases the free volume in the polymer matrix, whereas KHFPSI consists of a fluorinated cycle that restricts mobility of the sulfonylimide group [42]. Chemical structures of salts were confirmed using ^{19}F NMR and IR analysis. All spectra are shown in Supplementary information (Figs. S1–6).

Thermal stability of the salts was investigated by TGA. As can be seen from Fig. 1B, KFSI demonstrates the lowest thermal stability and degradation started already at around 200 °C due to the labile F–S bond. It is generally known that the FSI^- anion possesses lower electrochemical and thermal stability in comparison with $TFSI^-$ anion [27]. KNFBSI and KHFPSI both demonstrate high thermal stability with start

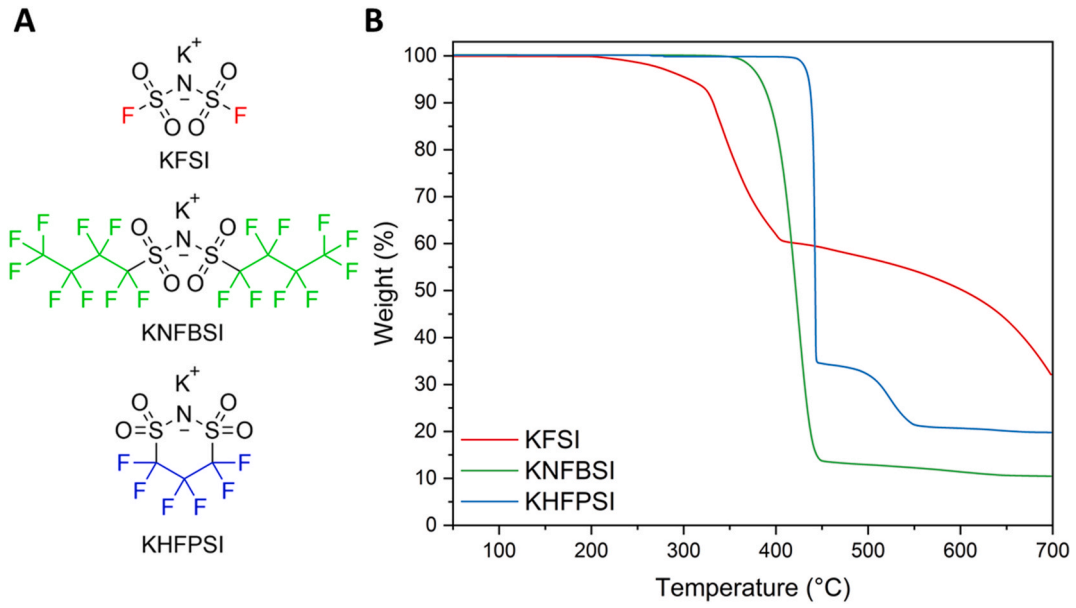


Fig. 1. Chemical structures (A) and TGA (B) curves of KFSI, KNFBSI and KHFPSI.

of decomposition at 360 °C and 420 °C, respectively, and therefore improve thermal stability of corresponding SPEs. The obtained TGA results are therefore in good agreement with previously reported data by Hu et al. [43].

After confirming the chemical structures of the salts, SPEs with PEO were prepared. All salts showed good solubility in acetonitrile and formed homogeneous, transparent films with PEO in a broad range of compositions.

3.2. Thermal properties of PEO-salt complexes

The SPEs films of sample series of PEO-salt complexes, PEO_x-$K(A)_y$ (x:y corresponded to EO:K molar ratios between 20:1, 18:1, 16:1, 12:1; and A represents the anions FSI, HFPSI or NFBSI), were investigated by DSC. The results are summarized in Table 1, and representative curves for PEO_{18}-$KFSI_1$, PEO_{16}-$KNFBSI_1$, and PEO_{16}-$KHFPSI_1$ are shown in Fig. 2A. Since these compositions exhibited highest ionic conductivities, they were therefore selected for further investigation described in subsequent sections.

Despite differences in salt structures, all SPE compositions displayed several common features. For example, the degree of crystallinity (X_c), which was calculated from the melting enthalpy using Equation (1) and provided in the Experimental Section, gradually decreased with increasing salt concentration. The SPE with KFSI at a 20:1 ratio showed a glass transition at −35 °C, followed by an exothermic cold-crystallization peak and two overlapping endothermic peaks with maxima at 40 °C and 53 °C, corresponding to melting of crystalline phases (Fig. S7). A two-step melting behavior in PEO-based SPEs has previously been reported for systems containing potassium and lithium salts [27,38] and is often associated with melting of eutectic PEO:salt domains of different compositions. Upon increasing the salt concentration, the first endothermic peak became less pronounced, and at a 14:1 ratio only a single melting peak remained at 44 °C. At this concentration, a dramatic drop in X_c occurred, accompanied by a shift of the glass-transition temperature to −40 °C.

Similarly, SPEs with KNFBSI exhibited two melting maxima in the

Table 1
Thermal properties of PEO–salt electrolytes obtained from DSC measurements.

Salt	Ratio	T_g (°C)[a]	Δ C_p (J g^{-1} K^{-1})	T_{m1} (°C)[b]	T_{m2} (°C)[b]	f_{peo}[c]	ΔH_c (J/g)[d]	ΔH_m (J/g)[e]	X_c (%)[f]
KFSI	20:1	−34.9	0.142	40	56	0.80	2.9	64.5	39.2
KFSI	18:1	−36.7	0.3	40	53	0.78	5.7	58.8	34.6
KFSI	16:1	−35.7	0.159	40	50	0.76	6.0	55.0	32.8
KFSI	14:1	−40.4	0.332	44	-	0.74	31.4	40.8	6.5
KFSI	12:1	−40.7	0.341	44	-	0.71	30.5	38.1	5.5
KNFBSI	20:1	-	-	62	-	0.59	-	55.2	47.6
KNFBSI	18:1	-	-	42	60	0.56	-	44.0	40.1
KNFBSI	16:1	-	-	42	57	0.53	-	35.8	34.4
KNFBSI	14:1	-	-	45	54	0.50	5.1	25.7	21.0
KNFBSI	12:1	−41.6	0.073	45	-	0.46	13.2	13.3	0.1
KHFPSI	20:1	−26.9	0.125	57	-	0.73	-	59.1	41.2
KHFPSI	18:1	−28.2	0.272	54	-	0.71	-	45.3	32.5
KHFPSI	16:1	−42.0	0.318	49	-	0.68	24.3	27.3	2.3
KHFPSI	14:1	−38.8	0.407	45	-	0.65	6.9	7.3	0.4
KHFPSI	12:1	−35.1	0.213	-	-	0.61	-	-	-

[a] Glass transition temperature T_g.
[b] First and second melting peak maximum temperature T_m.
[c] Mass fraction of PEO in SPE f_{peo}.
[d] Enthalpy of cold crystallization ΔH_c.
[e] Enthalpy of melting ΔH_m.
[f] Degree of crystallinity X_c.

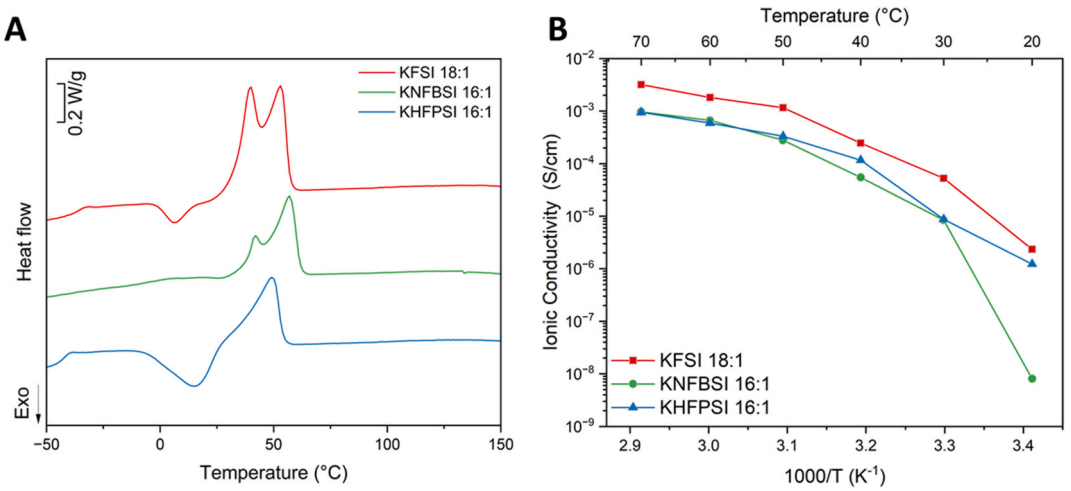


Fig. 2. DSC curves (A) and temperature dependence of ionic conductivity (B) of PEO based SPE with 18:1 KFSI, 16:1 KNFBSI and 16:1 KHFPSI.

range of 18:1 to 14:1 compositions (Fig. S8). However, at the highest ratio (20:1), only a single high-temperature melting peak at 62 °C was observed, whereas at the lowest ratio (12:1) only one melting peak at 45 °C appeared. No glass transition or cold crystallization could be detected due to rapid crystallization kinetics in the KNFBSI-based SPEs. Only at the 12:1 ratio, where the X_c approached zero, a glass-transition temperature became apparent at −41 °C. In contrast to the other salts, KHFPSI exhibited only one melting peak at all polymer–salt ratios. The high-temperature melting peak gradually decreased from 57 °C to 45 °C with increasing salt concentration, and at the 12:1 ratio no endothermic melting peak remained, indicating complete amorphization of the polymer (Fig. S9). SPEs with KHFPSI also showed the higher glass-transition temperatures (−27 to −28 °C at 20:1 and 18:1 correspondingly), likely due to the relatively high melting points of these compositions (54–57 °C). At the 16:1 ratio, the melting point decreased to 49 °C and the glass-transition temperature dropped to −42 °C. Further increases in salt concentration led to a rise in T_g, which can be attributed to the formation of quasi-ionic cross-links.

3.3. Ionic conductivities

The ionic conductivity of SPEs containing different salts was measured in the temperature range of 20–70 °C using electrochemical impedance spectroscopy (EIS). For each salt, the composition exhibiting the highest ionic conductivity was selected for further analysis. The corresponding temperature dependence of ionic conductivity is shown in Fig. 2B. The conductivity data for all other compositions are provided in the Supplementary Information (Fig. S10). At temperatures above the melting point (60 °C), SPEs containing each of the three investigated salts exhibited high ionic conductivities on the order of 10^{-3} S cm^{-1}, comparable to values reported for potassium bis(trifluoromethanesulfonyl)imide (KTFSI) [38]. Upon decreasing the temperature, progressive crystallization of the polymer matrix occurred, which restricts polymer segmental mobility and consequently reduces ionic conductivity. At 20 °C, the SPE containing KNFBSI exhibited an ionic conductivity two orders of magnitude lower than that of the other salts. This pronounced decrease may be attributed to the formation of additional crystalline phases with limited ionic transport. It is likely that a large fraction of the KNFBSI salt remained crystalline, reducing the number of mobile charge carriers in the amorphous phase and thereby leading to a significant drop in conductivity. With increasing temperature, the differences in ionic conductivity between the salts became less pronounced due to enhanced segmental mobility and partial melting of crystalline domains. For all three salts, the same general trend was observed. At low salt concentrations, the ionic conductivity increased with increasing salt content due to the higher number of charge carriers. Beyond a certain concentration, however, the conductivity reached a maximum and then slightly decreased, which could be attributed to the formation of physical cross-links within the polymer matrix. The position of this conductivity maximum differed between the systems: for KFSI, the optimal composition was EO:K = 18:1, whereas for KNFBSI and KHFPSI it is EO:K = 16:1. These optimal compositions were subsequently investigated in more detail. Nevertheless, the KFSI-based SPE consistently exhibited the highest ionic conductivity, which could be attributed to the smaller anion size and its higher mobility, whereas the KNFBSI-based SPE showed significantly reduced conductivity below melting temperature.

3.4. Temperature-dependent XRD of PEO–salt complexes

To further investigate the crystalline structure of the SPEs, XRD measurements were performed in the temperature range of 20–60 °C. As an example, the XRD diffractograms recorded at 20 °C for all SPEs at a selected EO:salt ratio are shown in Fig. 3. For all SPEs, two distinct features are observed: a single peak at 6.9° and a triplet at approximately 8.3°, which are attributed to crystalline reflections of PEO. These results are in good agreement with previously reported data obtained

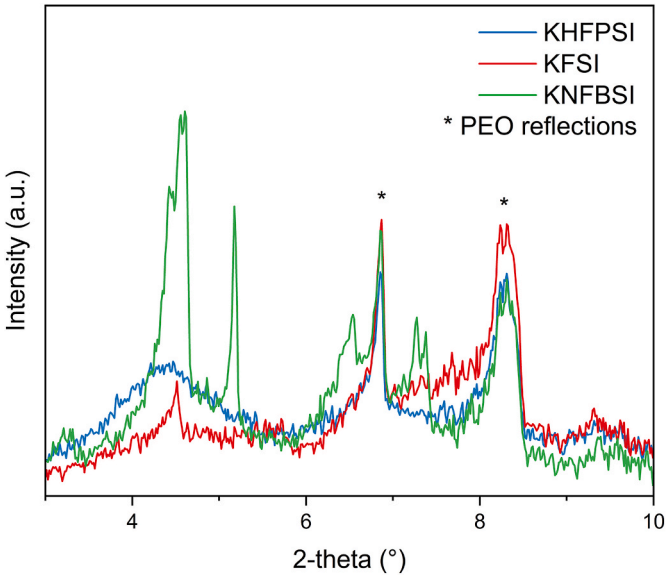


Fig. 3. XRD diffractograms of SPEs with different salts at 20 °C.

using Cu-Kα radiation, where PEO exhibits characteristic reflections at 19.08° and 23.19° [44]. Additionally, Rietveld refinement was applied to the diffraction patterns recorded at 20 °C to assign the observed reflections to crystalline PEO, as shown in the Supplementary Information (Fig. S11–S13). The diffraction pattern of the KHFPSI-based SPE contains only reflections that can be attributed to the crystalline PEO phase. In contrast, additional reflections are observed for the KNFBSI- and KFSI-based SPEs, indicating the presence of secondary crystalline phases formed by PEO and the corresponding potassium salts [45]. These observations are consistent with the DSC results, where KFSI- and KNFBSI-based SPEs exhibit a two-step melting process, whereas the KHFPSI-based SPE shows a single melting transition.

The XRD diffractograms of the KHFPSI-based SPE recorded at temperatures between 20 and 60 °C are shown in Fig. S14. Upon increasing the temperature from 20 to 30 °C, the degree of crystallinity slightly increased due to continued crystallization. With further increase in temperature, the intensity of the PEO reflections gradually decreased, and the reflections disappeared completely at 50 °C. This observation correlated well with the DSC data, where a melting temperature of 49 °C was observed. At temperatures above 50 °C, only an amorphous halo was present, indicating that the sample became fully amorphous. The SPEs containing KFSI and KNFBSI exhibited similar behavior, as shown in the Supplementary Information (Figs. S15 and S16). The KFSI-containing SPE displayed the same characteristic crystalline PEO reflections; however, additional reflections at 4.5°, 5.6°, 6.5°, and 9.3° were observed, which could not be attributed to the diffraction pattern of pure KFSI salt.

It is known for the PEO–LiTFSI systems that, in addition to crystalline and amorphous PEO phases, a secondary crystalline phase with an EO:Li ratio of 6:1 can form, as identified by XRD, Raman spectroscopy, and optical microscopy [36,46]. Similar behavior has been reported for the PEO–KTFSI system, where crystalline phases with EO:K ratios of 10:1 and 1.5:1 have been identified [45]. As discussed in the previous section, the DSC thermogram of the PEO–KFSI sample exhibited two melting transitions at 40 and 53 °C. Therefore, the additional reflections observed in the XRD patterns may be associated with the formation of a secondary crystalline phase consisting of a PEO–KFSI complex. Upon increasing the temperature to the first melting transition at 40 °C, these additional reflections disappeared, leaving only the reflections corresponding to crystalline PEO. This indicates that the low-temperature melting transition is associated with the melting of a secondary PEO–KFSI crystalline phase. The diffractograms of the KNFBSI-containing SPE exhibited, in addition to the PEO reflections, additional reflections at 4.6°, 5.2°, 6.5°, and 7.3°. These reflections may also be attributed to a secondary crystalline phase formed by a PEO–KNFBSI complex, as they were absent in the diffractogram of pure KNFBSI. In contrast to the PEO–KFSI system, the intensity of the reflections assigned to this secondary phase was higher than that of the PEO reflections, indicating that a significant fraction of KNFBSI remained in a crystalline state. With increasing temperature, the intensity of all crystalline reflections decreased, reflecting a reduction in the degree of crystallinity X_c. Same as for KFSI, above the first melting point (50 °C), only the crystalline phase of PEO remained detectable. The X_c was estimated for all samples by dividing the integrated area of the crystalline reflections by the total scattered area using Equation (2) described in the *Experimental section*. The corresponding values are summarized in Table S1, highlighting the dramatic drop in the degree of crystallinity after the melting of secondary crystalline phase.

3.5. Pulsed-field gradient NMR analysis

To gain more insight of how different anions influence ion transport in SPEs, pulsed-field gradient (PFG) NMR was employed to determine self-diffusion coefficients and effective activation energies of ion conduction at various temperatures. Due to the low resonance frequency and the corresponding sensitivity of ^{39}K, the measurements were performed using ^{19}F nuclei, which serve as a reliable probe for anion mobility. This approach is supported by the previous study on PEO-based block copolymers containing LiTFSI, where we could successfully show that comparable activation energies can be obtained from diffusion coefficients derived from both ^{7}Li and ^{19}F NMR measurements [47]. Therefore, ^{19}F NMR provides a suitable method for evaluating ion transport behavior in the present systems. The dependence of echo intensity on the gradient field strength in the temperature range from 27 to 67 °C in steps of 5 °C was measured for KFSI 1:18, KNFBSI 1:16 and KHFPSI 1:16 (Fig. S17–S19 in Supplementary information). The temperature dependence of the diffusion coefficients (ln D vs. 1/T) is shown in Fig. 4. All samples exhibited Vogel–Tammann–Fulcher (VTF) behavior with a change in slope in the temperature range corresponding to the melting transition. Effective activation energies were calculated using the VTF equation for the regions below and above the melting point and results are shown in the Supplementary Information (Table S2). Since the assumption of a single temperature-independent activation energy is not valid within the melting region, no activation energies were determined in this region. These results are consistent with the ionic conductivity data, which show that KFSI has the lowest effective activation energy, while KNFBSI exhibits the highest.

Both KFSI- and KNFBSI-based SPEs exhibited three distinct regions: below the melting point (27–37 °C), during the melting of crystalline phases (42–52 °C), and above the melting transition. In contrast, the KHFPSI-based SPE showed only two regions - below and above 52 °C - due to the presence of a single melting transition. The effective activation energy calculated above the melting temperature decreased with increasing ionic conductivity in the order KFSI > KHFPSI > KNFBSI. Additionally, the ^{19}F NMR spectra of KNFBSI-based SPEs reveal contributions from two types of ^{19}F species: a broad signal associated with fluorinated species exhibiting slow or restricted motion, and sharp signals corresponding to mobile ions, only the latter species were analyzed with PFG NMR. Therefore, the results for diffusion coefficients of KNFBSI-based SPE below the first melting temperature only represent the mobile ions. With increasing temperature, the integral area of the broad component became less pronounced, and only the sharp signals remained above the melting temperature of 57 °C. The respective spectra are shown in the Supporting information (Fig. S20). As the presence of multiple crystalline phases has been confirmed by XRD, the immobile species were likely associated with these phases.

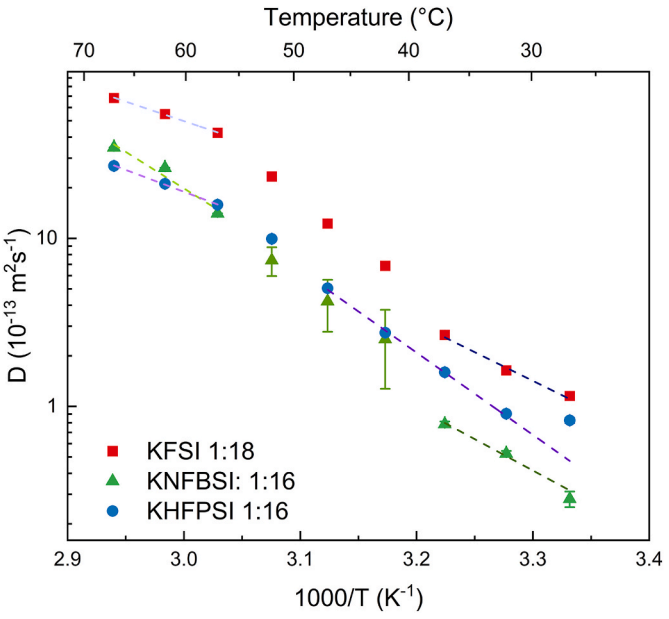


Fig. 4. Temperature dependence of diffusion coefficients for SPEs with different salts.

Consequently, the low ionic conductivity of KNFBSI-based SPEs at low temperatures can be attributed to the presence of secondary crystalline phases with limited ionic transport. With increasing temperature and a corresponding decrease in crystallinity, the contribution of immobile species diminished, leading to improved ion transport.

3.6. Electrochemical stability and cycling performance

The electrochemical stability of SPEs containing different salts was investigated using LSV, and the results are shown in Fig. S21. A two-step decomposition has been previously reported for PEO-based SPEs containing KFSI [48]. The FSI anion is known to have low electrochemical stability and decomposes at relatively low potentials due to the labile S–F bond. KHFPSI exhibited a similar decomposition behavior, however, the observed current was lower compared to KFSI, reflecting the higher stability of the KHFPSI anion. Among all investigated salts, KNFBSI showed the least pronounced first decomposition step and the lowest current, indicating the highest electrochemical stability.

Finally, the electrochemical performance of SPEs was evaluated in coin cells with $K_2Fe[Fe(CN)_6]$-based positive electrodes and potassium metal as negative electrode. To avoid melting of potassium metal electrode ($T_m = 63\,^{\circ}C$) and maintain reasonable ionic conductivity, cells were cycled at 55 °C. The galvanostatic profiles of the SPE with KFSI are shown in Fig. 5A, exhibiting two pronounced plateaus at 3.4 and 4.0 V,

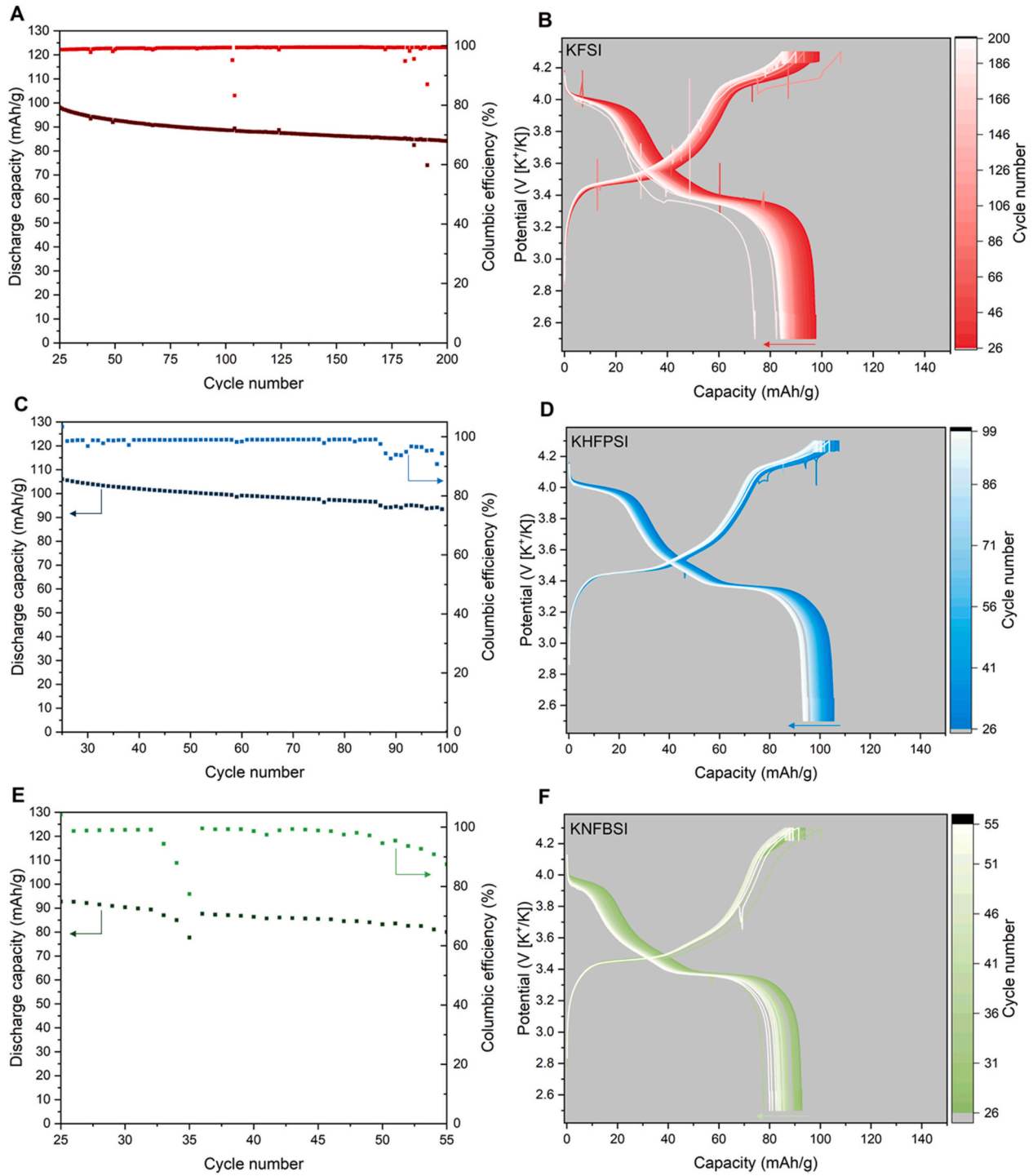


Fig. 5. Charge–discharge profiles and cycling performance of half-cells containing SPEs with KFSI (A–B), KNFBSI (C–D), and KHFPSI (E–F).

characteristic for $K_2Fe[Fe(CN)_6]$ [38]. For all cells, the C-rate tests were performed followed by long-term cycling at C/10. C-rate tests are provided in Supplementary Information (Fig. S22–24).

It is known that the degradation products of FSI^- form stable SEI that stabilize the interphase enabling a discharge capacity of 84 mAh/g after 200 cycles with 84% capacity retention and an average coulombic efficiency of ~99.5% [49,50]. During first cycle at C/10, the cell exhibited discharge capacity of 102 mAh/g that is around 65% out of theoretical capacity. Columbic efficiency gradually increased from 90% in the first cycle to 99% at the 11th cycle. After switching back to C/10 following the rate test, the discharge capacity remained at 98 mAh/g indicating good reversibility. The corresponding charge–discharge profiles of long-term cycling at C/10 (Fig. 5B) showed a slight increase in overpotential during cycling, leading to a gradual decrease in discharge capacity. In contrast, KNFBSI and KHFPSI exhibited higher coulombic efficiencies during rate testing, consistent with their improved electrochemical stability at high potentials. Despite the good electrochemical stability indicated by LSV, KNFBSI showed a coulombic efficiency of ~99% and a faster capacity fade upon cycling, likely due to lower ionic conductivity, strong tendency for recrystallization and higher polarization.

As shown in the charge–discharge curves (Fig. 5F), KNFBSI exhibited more pronounced capacity fading compared with the other systems. Notably, the first plateau at 3.4 V remained almost unchanged, whereas the second plateau at approximately 4.0 V becomes significantly shorter and shifts upon cycling. The shortening of the upper plateau is likely caused by increased polarization, as evidenced by the pronounced increase in overpotential. By the 26th cycle, the upper plateau during discharge dropped below 4.0 V for KNFBSI-based cell, whereas it remained approximately 50 mV higher for the other systems. This increased polarization likely contributes to the lower discharge capacity and accelerated capacity fading. Although KHFPSI delivered the highest initial discharge capacity of 109 mAh/g and a coulombic efficiency of ~99%, the cell could be cycled for fewer than 100 cycles, indicating higher degrees of parasitic processes. The charge–discharge profiles of the KHFPSI-based cell showed a behavior similar to that of the KFSI-based cell, with increasing polarization during cycling accompanied by more rapid capacity fading.

4. Conclusions

In this study, the effect of potassium salt anions on the structural, transport, and electrochemical properties of PEO-based solid polymer electrolytes was systematically investigated. It was shown that the choice of anion strongly affects the crystallinity of the polymer matrix, the formation of additional salt–polymer crystalline phases, and consequently the ion transport properties. All investigated systems exhibited decreasing crystallinity with increasing salt concentration; however, KHFPSI enabled nearly complete amorphization of PEO at high salt loadings. While all SPEs demonstrated comparable ionic conductivities on the order of 10^{-3} S cm^{-1} at elevated temperatures, pronounced differences were observed at lower temperatures. In particular, KNFBSI-based SPEs showed significantly reduced ionic conductivity, which was attributed to the formation of additional crystalline phases that limit both polymer segmental mobility and the number of mobile charge carriers. PFG NMR analysis as well as the line shape in ^{19}F spectra confirmed the presence of immobile ionic species in KNFBSI-containing systems, supporting the proposed mechanism of hindered ion transport. In contrast, KFSI-based SPEs exhibited the highest ionic conductivity due to favorable ion dissociation and anion mobility, although at the cost of reduced electrochemical stability. KHFPSI represented an intermediate case, combining improved thermal and electrochemical stability with moderate transport properties. Overall, this work demonstrates that the anion structure plays a key role in determining the structure–transport relationships in SPEs. These insights provide important guidelines for the rational design of advanced solid polymer electrolytes for high-performance potassium metal batteries.

CRediT authorship contribution statement

Timofey I. Kolesnikov: Writing – review & editing, Writing – original draft, Visualization, Validation, Methodology, Investigation, Data curation, Conceptualization. **Hongyuan Yu:** Writing – review & editing, Methodology, Investigation, Data curation. **Ramon Zimmermanns:** Writing – review & editing, Investigation. **Mareen Schaller:** Writing – review & editing, Investigation, Data curation. **Liuda Mereacre:** Writing – review & editing, Methodology. **Arseniy Bokov:** Writing – review & editing, Methodology. **Sylvio Indris:** Writing – review & editing, Supervision. **Michael Knapp:** Writing – review & editing, Supervision. **Patrick Theato:** Writing – review & editing, Supervision, Project administration. **Fabian Jeschull:** Writing – review & editing, Supervision, Project administration, Conceptualization.

Declaration of generative AI use

During the preparation of this work, the authors used ChatGPT to assist with language editing and proofreading of the manuscript and to generate an initial image for the graphical abstract. After using this tool, the authors reviewed and edited the content as needed and take full responsibility for the content of the published article.

Declaration of competing interest

The authors declare that they have no known competing financial interests or personal relationships that could have appeared to influence the work reported in this paper.

Acknowledgements

This work contributes to the research performed at CELEST (Center for Electrochemical Energy Storage Ulm-Karlsruhe) and was funded by the German Research Foundation (DFG) under Project ID 390874152 (POLiS Cluster of Excellence). T.K. acknowledges research funding through the DFG project 562331271. H.Y. acknowledges research funding through the China Scholarship Council project 202306250032. The authors gratefully acknowledge Benjamin Brecht for his assistance with the experimental work.

Open Access funding enabled and organized by Projekt DEAL.

Appendix A. Supplementary data

Supplementary data to this article can be found online at https://doi.org/10.1016/j.jpowsour.2026.241946.

Data availability

The data supporting the findings presented in this study are openly available in the Zenodo repository at https://doi.org/10.5281/zenodo.21933992.

References

[1] K. Kubota, M. Dahbi, T. Hosaka, S. Kumakura, S. Komaba, Towards K-Ion and Na-Ion batteries as "Beyond Li-Ion,", Chem. Rec. 18 (2018) 459–479, https://doi.org/10.1002/tcr.201700057.

[2] Y. Tian, G. Zeng, A. Rutt, T. Shi, H. Kim, J. Wang, J. Koettgen, Y. Sun, B. Ouyang, T. Chen, Z. Lun, Z. Rong, K. Persson, G. Ceder, Promises and challenges of next-generation "Beyond Li-ion" batteries for electric vehicles and grid decarbonization, Chem. Rev. 121 (2021) 1623–1669, https://doi.org/10.1021/acs.chemrev.0c00767.

[3] X. Min, J. Xiao, M. Fang, W. (Alex) Wang, Y. Zhao, Y. Liu, A.M. Abdelkader, K. Xi, R.V. Kumar, Z. Huang, Potassium-ion batteries: outlook on present and future technologies, Energy Environ. Sci. 14 (2021) 2186–2243, https://doi.org/10.1039/D0EE02917C.

[4] R. Rajagopalan, Y. Tang, X. Ji, C. Jia, H. Wang, Advancements and challenges in potassium ion batteries: a comprehensive review, Adv. Funct. Mater. 30 (2020), https://doi.org/10.1002/adfm.201909486.
[5] T. Hosaka, K. Kubota, A.S. Hameed, S. Komaba, Research development on K-ion batteries, Chem. Rev. 120 (2020) 6358–6466, https://doi.org/10.1021/acs.chemrev.9b00463.
[6] V. Gabaudan, L. Monconduit, L. Stievano, R. Berthelot, Snapshot on negative electrode materials for potassium-ion batteries, Front. Energy Res. 7 (2019), https://doi.org/10.3389/fenrg.2019.00046.
[7] I. Panasenko, M. Bäuerle, F. Jeschull, How reference electrodes improve our understanding of degradation processes in half and full cell potassium-ion battery setups, Electrochim. Acta 513 (2025) 145551, https://doi.org/10.1016/j.electacta.2024.145551.
[8] S. Komaba, T. Hasegawa, M. Dahbi, K. Kubota, Potassium intercalation into graphite to realize high-voltage/high-power potassium-ion batteries and potassium-ion capacitors, Electrochem. Commun. 60 (2015) 172–175, https://doi.org/10.1016/j.elecom.2015.09.002.
[9] H. Wang, D. Zhai, F. Kang, Solid electrolyte interphase (SEI) in potassium ion batteries, Energy Environ. Sci. 13 (2020) 4583–4608, https://doi.org/10.1039/D0EE01638A.
[10] A. V, B. John, M. Td, Potassium-ion batteries: key to future large-scale energy storage? ACS Appl. Energy Mater. 3 (2020) 9478–9492, https://doi.org/10.1021/acsaem.0c01574.
[11] N. Dautain, J.-F. Martin, D. Sotta, P. Azais, D. Peralta, The tremendous challenge of suitable KPF6-based electrolytes for 4 V-class K-metal cells, J. Power Sources 614 (2024) 234993, https://doi.org/10.1016/j.jpowsour.2024.234993.
[12] J. Zhang, X. Yao, R.K. Misra, Q. Cai, Y. Zhao, Progress in electrolytes for beyond-lithium-ion batteries, J. Mater. Sci. Technol. 44 (2020) 237–257, https://doi.org/10.1016/j.jmst.2020.01.017.
[13] H. Yin, C. Han, Q. Liu, F. Wu, F. Zhang, Y. Tang, Recent advances and perspectives on the polymer electrolytes for Sodium/Potassium-Ion batteries, Small 17 (2021), https://doi.org/10.1002/smll.202006627.
[14] J. Mindemark, M.J. Lacey, T. Bowden, D. Brandell, Beyond PEO—alternative host materials for Li + -conducting solid polymer electrolytes, Prog. Polym. Sci. 81 (2018) 114–143, https://doi.org/10.1016/j.progpolymsci.2017.12.004.
[15] S. Kundu, Y. Ein-Eli, A review on design considerations in polymer and polymer composite solid-state electrolytes for solid Li batteries, J. Power Sources 553 (2023) 232267, https://doi.org/10.1016/j.jpowsour.2022.232267.
[16] Z. Xue, D. He, X. Xie, Poly(ethylene oxide)-based electrolytes for lithium-ion batteries, J. Mater. Chem. A 3 (2015) 19218–19253, https://doi.org/10.1039/C5TA03471J.
[17] S. Kang, D. Setiawan, S.-T. Hong, H. Lee, A free-standing sulfone-based solid-state electrolyte mitigating the release of crystal water from the Prussian blue cathode for high voltage potassium batteries, J. Power Sources 631 (2025) 236299, https://doi.org/10.1016/j.jpowsour.2025.236299.
[18] Z. Zhou, Y. Yuan, X. Tang, W. Liu, B. Yang, J. Wen, L. Liu, Enhancing ionic conductivity of polyethylene oxide-based solid-state electrolytes through blending with a small amount of polyacrylic acid: a polymer-anion synergistic mechanism, J. Power Sources 644 (2025) 237132, https://doi.org/10.1016/j.jpowsour.2025.237132.
[19] D.E. Fenton, J.M. Parker, P.V. Wright, Complexes of alkali metal ions with poly (ethylene oxide), Polymer (Guildf.) 14 (1973) 589, https://doi.org/10.1016/0032-3861(73)90146-8.
[20] B. Sun, J. Mindemark, K. Edström, D. Brandell, Polycarbonate-based solid polymer electrolytes for Li-ion batteries, Solid State Ionics 262 (2014) 738–742, https://doi.org/10.1016/j.ssi.2013.08.014.
[21] J. Mu, S. Liao, L. Shi, B. Su, F. Xu, Z. Guo, H. Li, F. Wei, Solid-state polymer electrolytes in lithium batteries: latest progress and perspective, Polym. Chem. 15 (2024) 473–499, https://doi.org/10.1039/D3PY01311A.
[22] T. Kanbara, M. Inami, T. Yamamoto, New solid-state electric double-layer capacitor using poly(vinyl alcohol)-based polymer solid electrolyte, J. Power Sources 36 (1991) 87–93, https://doi.org/10.1016/0378-7753(91)80047-2.
[23] I.L. Johansson, T.I. Kolesnikov, A. Khudyshkina, U.-C. Rauska, D. Brandell, J. Mindemark, G. Hernández, F. Jeschull, Polycarbonate-based polymer electrolytes for potassium batteries, Solid State Ionics 432 (2025) 117069, https://doi.org/10.1016/j.ssi.2025.117069.
[24] U. Oteo, M. Martinez-Ibañez, I. Aldalur, E. Sanchez-Diez, J. Carrasco, M. Armand, H. Zhang, Improvement of the cationic transport in polymer electrolytes with (difluoromethanesulfonyl)(trifluoromethanesulfonyl)imide salts, Chemelectrochem 6 (2019) 1019–1022, https://doi.org/10.1002/celc.201801472.
[25] L.A. Schkeryantz, J. Zheng, W.D. McCulloch, L. Qin, S. Zhang, C.E. Moore, Y. Wu, Designing potassium battery salts through a solvent-in-anion concept for concentrated electrolytes and mimicking solvation structures, Chem. Mater. 32 (2020) 10423–10434, https://doi.org/10.1021/acs.chemmater.0c02983.
[26] J. Chen, S. Ebrahimi-Koodehi, B. Iliev, Y. Steinberg, M. Leskes, T.J.S. Schubert, E. Castillo-Martínez, D. Bresser, M. Zarrabeitia, Polymer electrolytes for potassium batteries: incorporating ionic liquids to enhance the room temperature ionic conductivity, J. Mater. Chem. A 13 (2025) 25476–25488, https://doi.org/10.1039/D5TA02762D.
[27] H. Zhang, C. Liu, L. Zheng, F. Xu, W. Feng, H. Li, X. Huang, M. Armand, J. Nie, Z. Zhou, Lithium bis(fluorosulfonyl)imide/poly(ethylene oxide) polymer electrolyte, Electrochim. Acta 133 (2014) 529–538, https://doi.org/10.1016/j.electacta.2014.04.099.
[28] Y. Pan, H. Yu, Y. Zhang, Z. Wang, S. Wang, C. Li, Y. Ma, X. Shi, H. Zhang, D. Song, L. Zhang, In-depth exploration of the effect mechanisms of various lithium salt anions in solid-state and liquid lithium metal batteries, J. Mater. Chem. A 12 (2024) 16447–16456, https://doi.org/10.1039/D4TA01939C.
[29] L. Deng, Y. Zhang, R. Wang, M. Feng, X. Niu, L. Tan, Y. Zhu, Influence of KPF 6 and KFSI on the performance of anode materials for potassium-ion batteries: a case study of MoS 2, ACS Appl. Mater. Interfaces 11 (2019) 22449–22456, https://doi.org/10.1021/acsami.9b06156.
[30] J. Liu, X. Shi, B. Tan, H. Zhang, J. Liu, H. Kang, Z. Gao, L. Li, Guidance KPF 6 - and KFSI-based electrolytes in EC/DEC solvents selection for potassium-based batteries, Nano Res. 19 (2026) 94908196, https://doi.org/10.26599/NR.2025.94908196.
[31] J. Xie, J. Li, W. Zhuo, W. Mai, Recent progress of electrode materials cooperated with potassium bis(fluorosulfonyl)imide–containing electrolyte for K-ion batteries, Mater. Today Adv. 6 (2020) 100035, https://doi.org/10.1016/j.mtadv.2019.100035.
[32] W. Lyu, H. Fu, A.M. Rao, Z. Lu, X. Yu, Y. Lin, J. Zhou, B. Lu, Permeable void-free interface for all-solid-state alkali-ion polymer batteries, Sci. Adv. 10 (2024), https://doi.org/10.1126/sciadv.adr9602.
[33] M. Jaipal Reddy, P.P. Chu, Optical microscopy and conductivity of poly(ethylene oxide) complexed with KI salt, Electrochim. Acta 47 (2002) 1189–1196, https://doi.org/10.1016/S0013-4686(01)00846-5.
[34] J.L. Olmedo-Martínez, L. Meabe, A. Basterretxea, D. Mecerreyes, A.J. Müller, Effect of chemical structure and salt concentration on the crystallization and ionic conductivity of aliphatic polyethers, Polymers 11 (2019) 452, https://doi.org/10.3390/polym11030452.
[35] M. Elmanzalawy, E. Sanchez-Ahijón, O. Kisacik, J. Carretero-González, E. Castillo-Martínez, High conductivity in a fluorine-free K-ion polymer electrolyte, ACS Appl. Energy Mater. 5 (2022) 9009–9019, https://doi.org/10.1021/acsaem.2c01485.
[36] M. Marzantowicz, J.R. Dygas, F. Krok, J.L. Nowiński, A. Tomaszewska, Z. Florjańczyk, E. Zygadło-Monikowska, Crystalline phases, morphology and conductivity of PEO:LiTFSI electrolytes in the eutectic region, J. Power Sources 159 (2006) 420–430, https://doi.org/10.1016/j.jpowsour.2006.02.044.
[37] B.-K. Choi, Y.-W. Kim, Conductivity relaxation in the PEO–salt polymer electrolytes, Electrochim. Acta 49 (2004) 2307–2313, https://doi.org/10.1016/j.electacta.2004.01.011.
[38] A.D. Khudyshkina, P.A. Morozova, A.J. Butzelaar, M. Hoffmann, M. Wilhelm, P. Theato, S.S. Fedotov, F. Jeschull, Poly(ethylene oxide)-Based electrolytes for solid-state potassium metal batteries with a Prussian Blue positive electrode, ACS Appl. Polym. Mater. 4 (2022) 2734–2746, https://doi.org/10.1021/acsapm.2c00014.
[39] G. Dreezen, M.H.J. Koch, H. Reynaers, G. Groeninckx, Miscible binary blends of poly(ethylene oxide) and an amorphous aromatic polyamide (Aramide 34I): crystallization, melting behavior and semi-crystalline morphology, Polymer (Guildf.) 40 (1999) 6451–6463, https://doi.org/10.1016/S0032-3861(98)00849-0.
[40] Netzsch, Crystallinity, Degree of Crystallinity - NETZSCH Analyzing & Testing, 2023. https://analyzing-testing.netzsch.com/en/know-how/glossary/crystallinity-degree-of-crystallinity. (Accessed 24 April 2026).
[41] E.O. Stejskal, J.E. Tanner, Spin diffusion measurements: spin echoes in the presence of a time-dependent field gradient, J. Chem. Phys. 42 (1965) 288–292, https://doi.org/10.1063/1.1695690.
[42] S. Buyting, M. Schönhoff, Enhanced Li transference in polymer electrolytes: why anion size affects cation mobility, ACS Appl. Polym. Mater. 7 (2025) 8432–8444, https://doi.org/10.1021/acsapm.5c00753.
[43] Y. Hu, L. Fan, A.M. Rao, W. Yu, C. Zhuoma, Y. Feng, Z. Qin, J. Zhou, B. Lu, Cyclic-anion salt for high-voltage stable potassium-metal batteries, Natl. Sci. Rev. 9 (2022), https://doi.org/10.1093/nsr/nwac134.
[44] Q.M. Al-Bataineh, I.A. Aljarrah, A.A. Ahmad, A.M. Alsaad, A. Telfah, Investigation of the doping mechanism and electron transition bands of PEO/KMnO4 complex composite films, J. Mater. Sci. Mater. Electron. 33 (2022) 14051–14062, https://doi.org/10.1007/s10854-022-08336-0.
[45] S. Lascaud, M. Perrier, A. Vallee, S. Besner, J. Prud'homme, M. Armand, Phase diagrams and conductivity behavior of Poly(ethylene oxide)-Molten Salt rubbery electrolytes, Macromolecules 27 (1994) 7469–7477, https://doi.org/10.1021/ma00103a034.
[46] M. Marzantowicz, J.R. Dygas, F. Krok, A. Tomaszewska, G.Z. Żukowska, Z. Florjańczyk, E. Zygadło-Monikowska, Phase segregation phenomena in poly (ethylene oxide):LiN(CF3SO2)2 electrolyte studied by local Raman spectroscopy, Electrochim. Acta 55 (2010) 5446–5452, https://doi.org/10.1016/j.electacta.2010.04.043.
[47] A.D. Khudyshkina, A.J. Butzelaar, Y. Guo, M. Hoffmann, T. Bergfeldt, M. Schaller, S. Indris, M. Wilhelm, P. Théato, F. Jeschull, From lithium to potassium: comparison of cations in poly(ethylene oxide)-based block copolymer electrolytes for solid-state alkali metal batteries, Electrochim. Acta 454 (2023) 142421, https://doi.org/10.1016/j.electacta.2023.142421.
[48] W. Lyu, X. Yu, Y. Lv, A.M. Rao, J. Zhou, B. Lu, Building stable solid-state potassium metal batteries, Adv. Mater. 36 (2024), https://doi.org/10.1002/adma.202305795.
[49] G.M.A. Girard, M. Hilder, N. Dupre, D. Guyomard, D. Nucciarone, K. Whitbread, S. Zavorine, M. Moser, M. Forsyth, D.R. MacFarlane, P.C. Howlett, Spectroscopic characterization of the SEI layer formed on lithium metal electrodes in Phosphonium Bis(fluorosulfonyl)imide ionic liquid electrolytes, ACS Appl. Mater. Interfaces 10 (2018) 6719–6729, https://doi.org/10.1021/acsami.7b18183.
[50] K. Hirata, Y. Morita, T. Kawase, Y. Sumida, Electrochemical performance of an ethylene carbonate-free electrolyte based on lithium bis(fluorosulfonyl)imide and sulfolane, J. Power Sources 395 (2018) 163–170, https://doi.org/10.1016/j.jpowsour.2018.05.059.